

# Phase-Rearrangement-Induced Atomic Replacement toward Customizing Noble-Metal Intermetallics

Xuan Huang,<sup>#</sup> Bingyan Xu,<sup>#</sup> Yang Sun,<sup>#</sup> Zhiyao Liang,<sup>#</sup> Changhong Zhan, Jiafeng Du, Xian-Kui Wei,\*  
Jie Feng, Youyong Li, Yujin Ji, Qi Shao,\* and Xiaoqing Huang\*



Cite This: <https://doi.org/10.1021/jacs.5c16486>



Read Online

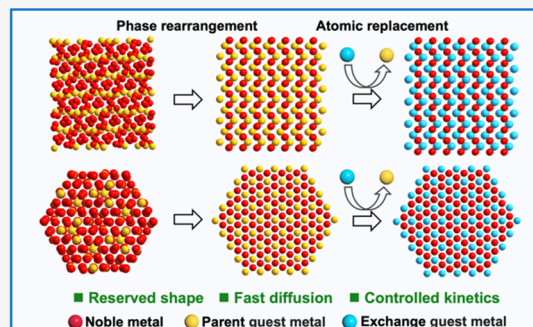
ACCESS |

Metrics & More

Article Recommendations

Supporting Information

**ABSTRACT:** Structurally controlled noble-metal intermetallics are promising for catalytic applications but are significantly hindered by the thermodynamically favored symmetric growth of close-packed structures and by differences in metal redox potentials. Here, we report a phase-rearrangement-induced atomic replacement synthesis in noble-metal chalcogenides that successfully realizes a nondestructive intermetallic nanoarchitecture. By choosing well-defined palladium–tellurium (Pd–Te) hexagonal nanoplates as parent templates, a morphology-preserved atomic replacement transformation from Te atoms to Bi atoms is achieved, enabling tunable compositions, phases, and interfaces at specific spatial locations. Mechanistic studies demonstrate that parent templates (rhombohedral phase Pd<sub>20</sub>Te<sub>7</sub>) undergo a phase rearrangement to the thermodynamically stable structure (hexagonal phase PdTe) prior to atomic replacement, effectively reducing lattice mismatch and permitting the atomic replacement process to occur while retaining the original morphology. This design rule is highly generalizable for a series of zero-, one-, and two-dimensional Pd–Bi (antimony (Sb), lead (Pb), and tin (Sn)) nanoarchitectures. Therefore, this work advances the diversity of materials and further investigates the potential effect of different phases and compositions on catalyst performance, in which the hexagonal phase PdBi exhibits superior oxygen reduction reaction activity, stability, and antipoisoning methanol capability. This generalizable atomic replacement strategy enables the exploration of heterostructures and intermetallic nanoarchitectures that are otherwise inaccessible.



## INTRODUCTION

The successful synthesis of noble metal-based intermetallic compounds (NM-IMCs) with controlled structures such as morphology, phase, composition, and even more complex interfaces has drawn extensive attention as NM-IMCs offer many opportunities to not only manipulate their physicochemical properties but also optimize their figure of merit in a wide variety of applications.<sup>1–4</sup> Simultaneously, the availability of NM-IMCs with well-defined and controllable structures provides new capabilities for the study of surface science and catalysis, further providing well-defined modeling systems for structure-performance mechanism studies.<sup>5–8</sup>

Extensive research over the past few decades has focused on establishing diverse synthetic strategies for NM-IMCs.<sup>9–12</sup> However, conventional wet-chemical methods usually form a thermodynamically stable state with particle morphology, as the dense stacking arrangement of the noble metals results in a highly symmetric crystal structure.<sup>13–15</sup> Template-based synthesis, whether employing hard or soft templates, provides an alternative approach for generating NM-IMCs.<sup>16,17</sup> However, template strategies are generally limited to noble-metal hosts of NM-IMCs.<sup>18,19</sup> For example, choosing Sn NPs as templates could only yield MSn<sub>4</sub> (M = Pt, Pd, Rh) due to differences in

redox potentials.<sup>20</sup> Moreover, selecting appropriate guest metals for NM-IMCs is equally crucial, and the regulation of the guest metal can influence the intrinsic properties of the central noble metal and thus optimize the catalytic performance.<sup>21–23</sup> Therefore, a broadly applicable synthetic approach is urgently needed that can overcome the symmetry-governed growth of NM-IMCs and the challenges arising from differences in metal redox potentials, enabling the controlled synthesis of NM-IMCs incorporating a wide range of guest metals.

Here, we demonstrate a universal and phase-rearrangement-induced atomic replacement synthesis in noble-metal chalcogenides to prepare NM-IMCs with controllable morphology, phase, composition, and interfaces. Te-based materials, with weak M-Te bonds allowing structural rearrangement and transformations, provide an excellent platform for the

Received: September 19, 2025

Revised: November 22, 2025

Accepted: November 25, 2025

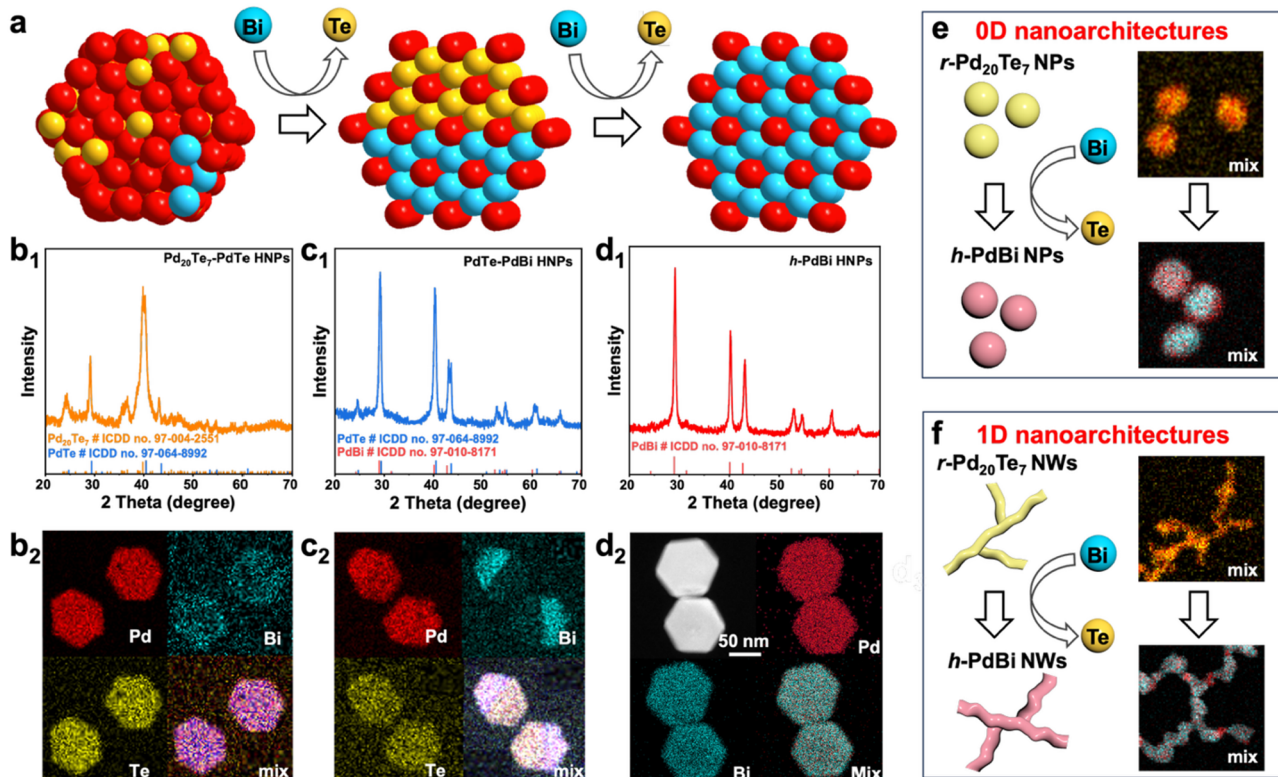


**Figure 1.** Atomic replacement for the transformation from  $r\text{-Pd}_{20}\text{Te}_7$  to  $h\text{-PdBi}$ . (a) Schematic structural evolution of  $r\text{-Pd}_{20}\text{Te}_7$  HNPs during complete transformation to  $h\text{-PdBi}$  HNPs (the extent of partial atomic replacement can be tuned by adjusting the Bi contents). The red, yellow, and blue balls represent Pd, Te, and Bi atoms. Characterizations of (b)  $\text{Pd}_{20}\text{Te}_7\text{-PdTe}$  HNPs with low Bi contents, (c)  $\text{PdTe-PdBi}$  HNPs with high Bi contents, and (d)  $h\text{-PdBi}$  HNPs with excessive Bi contents: (b<sub>1</sub>, c<sub>1</sub>, d<sub>1</sub>) XRD patterns, and (b<sub>2</sub>, c<sub>2</sub>, d<sub>2</sub>) elemental mappings. Atomic replacement for complete transformation from (e)  $r\text{-Pd}_{20}\text{Te}_7$  NPs to  $h\text{-PdBi}$  NPs and (f)  $r\text{-Pd}_{20}\text{Te}_7$  NWs to  $h\text{-PdBi}$  NWs.

formation and development of diverse intermetallic materials. Starting from rhombohedral phase  $Pd_{20}Te_7$  ( $r\text{-Pd}_{20}\text{Te}_7$ ) as a template, the atomic replacement between Te atoms and bismuth (Bi) atoms is carried out while preserving the morphology. Mechanistic studies reveal that  $r\text{-Pd}_{20}\text{Te}_7$  undergoes phase rearrangement to the thermodynamically more stable structure (hexagonal phase  $\text{PdTe}$ ) to release the atomic replacement interfacial strain.<sup>24,25</sup> Additionally, the generality of this atomic-replacement strategy can be validated by multiple phases<sup>26</sup> (from  $r\text{-Pd}_{20}\text{Te}_7$  to cubic phase  $\text{Pd}_4\text{Te}$ , and rhombohedral phase  $\text{Pd}_8\text{Te}_3$ ), composition (Sb, Pb, and Sn atoms), and morphology regulations (from two-dimensional (2D) hexagonal nanoplates to 0D nanoparticles and 1D nanowires). The oxygen reduction reaction (ORR) was utilized as a proof-of-concept application to elucidate the phase- and composition-dependent performance of the synthesized intermetallic catalysts. Notably, the catalyst with a hexagonal phase and Pd–Bi composition exhibits excellent ORR activity (mass activity of  $1.54 \text{ A mg}_{\text{Pt}}^{-1}$ ), stability (negligible MA decay after 20,000 ADT cycles), and excellent antipoisoning methanol capability. This work paves the way for a phase-rearrangement-facilitated atomic replacement approach for the design and manufacture of inaccessible nanoscale multifunctional intermetallics.

## RESULTS AND DISCUSSION

**Atomic Replacement for Transformation from  $r\text{-Pd}_{20}\text{Te}_7$  to  $h\text{-PdBi}$ .** Here, we select rhombohedral phase  $Pd_{20}Te_7$  hexagonal nanoplates ( $r\text{-Pd}_{20}\text{Te}_7$  HNPs) as parent nanocrystals (see the Experimental Section in the Supporting

Information for complete experimental details). On the one hand, we challenge the traditional assumption by demonstrating that Te atoms exhibit higher mobility than Pd atoms and undergo significant spontaneous rearrangement.<sup>27</sup> On the other hand, the well-defined crystal facets and atomic arrangement of the HNPs favor the investigation of the directionality and selectivity of atomic replacement reactions. The X-ray diffraction (XRD) pattern of HNPs was examined (Figure S1a) and was consistent with that of  $r\text{-Pd}_{20}\text{Te}_7$  (ICDD no. 97-004-2551). Transmission electron microscopy (TEM) analyses reveal a uniform hexagonal nanoplate morphology (Figure S1b,c) with lateral size and average height (Figure S1d) of  $62.1 \times 17.5 \text{ nm}$ , respectively. Further examination by the high-resolution TEM (HRTEM) reveals that the diffraction pattern of the  $r\text{-Pd}_{20}\text{Te}_7$  HNPs is consistent with the [001] crystal axis in the  $R\bar{3}$  (148), and the exposed crystal facets are (001) facets.<sup>26</sup> The scanning electron microscopy energy-dispersive X-ray spectroscopy (SEM-EDS) characterization (Figure S1f) indicates a Pd:Te atomic ratio of 72.29:27.71 within the  $r\text{-Pd}_{20}\text{Te}_7$  HNPs. The centrifuged  $r\text{-Pd}_{20}\text{Te}_7$  HNPs were dispersed in a benzyl alcohol (BA) solution containing Bi precursors and subsequently maintained at  $200^\circ\text{C}$  for 3 h. The extent of atomic replacement could be controlled by adding different amounts of Bi precursors, named as  $\text{Pd}_{20}\text{Te}_7\text{-PdTe}$  HNPs,  $\text{PdTe-PdBi}$  HNPs, and  $h\text{-PdBi}$  HNPs, which enable broad tunability of the intrananoplate framework features while preserving the hexagonal nanoplate morphology. Figure 1a shows the gradual exchange between the Bi and Te atoms and the completion of the replacement process on the HNP templates. The morphology and

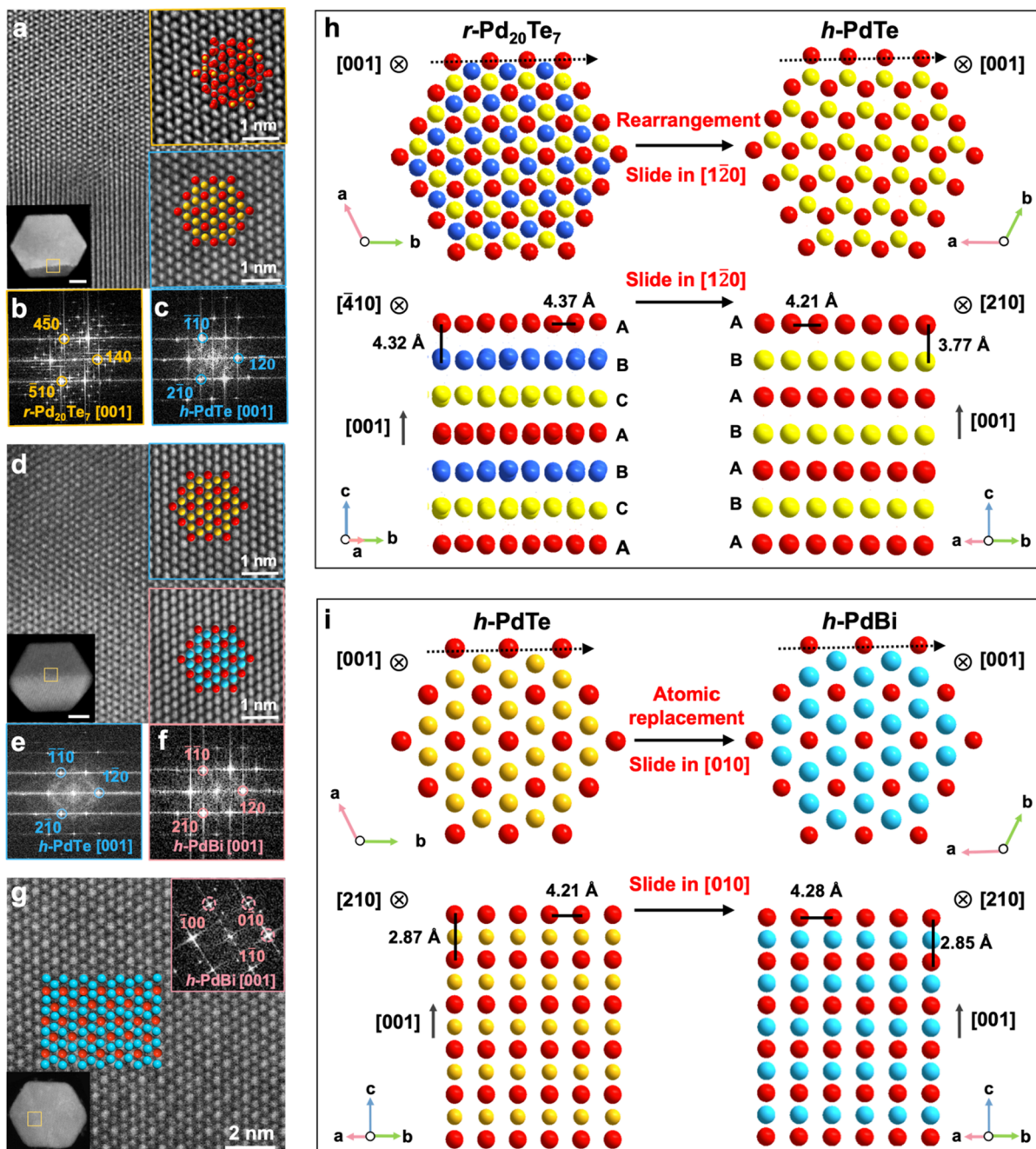


**Figure 2.** Detailed structure analysis of the transformation from  $r\text{-Pd}_{20}\text{Te}_7$  to  $h\text{-PdBi}$  HNPs. (a) Atomic-resolution HAADF-STEM image of  $\text{Pd}_{20}\text{Te}_7\text{-PdTe}$  HNPs and the corresponding atomic structure model (inset in (a)). (b,c) FFT images from the yellow and blue squares marked in (a). (d) Atomic-resolution HAADF-STEM image of PdTe-PdBi HNPs and the atomic structure model (inset in (d)). And (e,f) the corresponding FFT images from the blue and red squares in (d). (g) Atomic-resolution HAADF-STEM image of  $h\text{-PdBi}$  HNPs and the corresponding FFT image (inset in the upper right of (g)) and atomic structure model (inset in (g)). The red, yellow, and cyan balls represent Pd, Te, and Bi atoms. (h) Atomic schematic structural evolution of  $r\text{-Pd}_{20}\text{Te}_7$  HNPs transformation to  $h\text{-PdTe}$  HNPs during phase rearrangement. Left is stacking sequences of Te atoms in  $r\text{-Pd}_{20}\text{Te}_7$ . Right is stacking sequences of Te atoms in  $h\text{-PdTe}$ . Different colored spheres denote Te atoms at different layers. The dotted arrow indicates the sliding direction along the  $[1\bar{2}0]$  of  $r\text{-Pd}_{20}\text{Te}_7$ . Values for the tellurium spacing correspond to the  $a$  and  $c$  lattice parameters. (i) Atomic schematic structural evolution of  $r\text{-Pd}_{20}\text{Te}_7$  HNPs transformation to  $h\text{-PdBi}$  HNPs during atomic replacement. The red, yellow, and cyan spheres represent Pd, Te, and Bi atoms, respectively. The dotted arrow indicates the sliding direction along  $[010]$  of  $h\text{-PdTe}$ . Values for the palladium spacing corresponding to the  $a$  and  $c$  lattice parameters.

composition of  $\text{Pd}_{20}\text{Te}_7\text{-PdTe}$  HNPs were characterized (Figures 1b and S2). The peaks in the XRD pattern (Figure 1b<sub>1</sub>) are mainly assigned to  $r\text{-Pd}_{20}\text{Te}_7$  (ICDD 97-004-2551) and a few slight peaks point to hexagonal phase PdTe ( $h\text{-PdTe}$ ) (ICDD 97-064-8992), indicating that the exchange process had occurred. The scanning TEM (STEM) elemental

mapping analysis (Figure 1b<sub>2</sub>) and line-scan profiling analysis (Figure S3) along the radial direction (marked with a yellow arrow) of  $\text{Pd}_{20}\text{Te}_7\text{-PdTe}$  HNPs show that a small number of Bi atoms incorporate onto the HNPs. The incorporation of Bi atoms perturbs the original Pd–Te lattice of  $r\text{-Pd}_{20}\text{Te}_7$  and induces its structural rearrangement, leading to the partial

formation of *h*-PdTe domains. With an increasing Bi content, the influence of atomic replacement on the morphology and crystal structure also increases. Thus, PdTe-PdBi Janus HNPs are obtained (**Figures 1c** and **S4**), with a significant thickness difference across HNPs, which also points to the directionality of Bi atom exchange on *r*-Pd<sub>20</sub>Te<sub>7</sub> HNPs. Due to the similar crystal structures of hexagonal phase PdBi (*h*-PdBi) (ICDD no. 97-010-8171) and *h*-PdTe (ICDD no. 97-064-8992), the two main peaks overlap at around 40° and 43° in the XRD pattern, confirming the coexistence of *h*-PdBi and *h*-PdTe (**Figure 1c**). The STEM elemental mapping (**Figure 1c**) and line scan (**Figure S5**) further confirm that Bi atoms are unevenly distributed on the HNPs and are obviously enriched in half of the region. Continuing to add excessive Bi atoms transforms the *r*-Pd<sub>20</sub>Te<sub>7</sub> HNPs to a pure hexagonal structure with *h*-PdBi HNPs, confirmed by XRD pattern (**Figure 1d**). The obvious difference in thickness nearly disappears in the TEM images (**Figure S6**) and high-angle annular dark-field STEM (HAADF-STEM) image (**Figure 1d**). Furthermore, the STEM elemental mapping together with the corresponding line-scan profiles demonstrates an even distribution of Pd and Bi across the HNPs, with their atomic ratio approaching 1:1 (**Figure S7**). Additionally, we performed time-lapse experiments to track the atomic replacement trajectories of *r*-Pd<sub>20</sub>Te<sub>7</sub> HNPs transforming into *h*-PdBi HNPs (**Figure S8** and **Table S1**). The compositions and structures of the intermediates collected after different time intervals were analyzed by SEM-EDS profiles and XRD patterns. At the early reaction stage (10 min), the *r*-Pd<sub>20</sub>Te<sub>7</sub> diffraction peaks became weaker due to lattice distortion caused by Bi incorporation; by 20 min, a new reflection appeared near 28°, corresponding to the formation of *h*-PdTe; and by 45 min, the *r*-Pd<sub>20</sub>Te<sub>7</sub> peak at 36° disappeared completely, confirming the full conversion to *h*-PdTe. With prolonged reaction times (90–180 min), new XRD peaks consistent with *h*-PdBi emerged, completing the overall transformation from *r*-Pd<sub>20</sub>Te<sub>7</sub> to *h*-PdBi through an intermediate *h*-PdTe stage. These results reveal that Bi plays a continuous and essential role throughout the entire process, driving the progressive lattice reconstruction and phase evolution. At 300 min, no further structural evolution is observed, confirming completion of the atomic replacement (**Figure S9**). Therefore, *r*-Pd<sub>20</sub>Te<sub>7</sub> HNPs can be partially or completely replaced with Bi atoms, enabling broad tunability of heterostructures and intermetallics. Despite the different interfacial structures, the overall size and shape of the HNPs are retained both before and after the atomic replacement.

In addition to 2D intermetallics, we also successfully realized other 0D nanoparticles (NPs) and 1D nanowires (NWs) intermetallic structures via a phase-rearrangement-induced atomic replacement reaction (**Figure 1e,f**). The *r*-Pd<sub>20</sub>Te<sub>7</sub> NPs (**Figure S10**) and *r*-Pd<sub>20</sub>Te<sub>7</sub> NWs (**Figure S11**), which exhibit homogeneous Pd and Te distributions, were prepared and used as parent templates for atomic replacement. After the atomic replacement reaction (**Figures S12** and **S13**), the structural evolution from *r*-Pd<sub>20</sub>Te<sub>7</sub> to *h*-PdBi was clearly observed, while the original NP and NW morphologies were preserved. This behavior is consistent with the previously described transformation of the 2D *r*-Pd<sub>20</sub>Te<sub>7</sub> HNPs. Therefore, the atomic replacement strategy is effective for fabricating intermetallics with tailored morphologies, thereby significantly diversifying the intermetallic library.

#### Detailed Structure Analysis for Transformation from *r*-Pd<sub>20</sub>Te<sub>7</sub> to *h*-PdBi HNPs.

To further characterize the

interfacial details during atomic replacement, spherical aberration-corrected HAADF-STEM imaging was employed. The HAADF-STEM image (inset of **Figure 2a**) of Pd<sub>20</sub>Te<sub>7</sub>-PdTe HNPs confirms the presence of a distinct phase interface. The enlarged atomic-resolution HAADF-STEM image (**Figure 2a**) and the corresponding FFT analyses reveal two crystalline domains that correspond to the [001] region axis of *r*-Pd<sub>20</sub>Te<sub>7</sub> (**Figure 2b**) and the [001] region axis of *h*-PdTe (**Figure 2c**). Analysis of the corresponding intensity profiles extracted from the HAADF-STEM image (**Figure S14**) confirms a periodic atomic arrangement on both sides of the heterointerface, consistent with the lattice spacing of the (140) plane in *r*-Pd<sub>20</sub>Te<sub>7</sub> and the (1̄20) plane in *h*-PdTe. This suggests that phase rearrangement occurs before atomic replacement begins, forming a heterointerface of [001] (140) of *r*-Pd<sub>20</sub>Te<sub>7</sub> // [001] (1̄20) of *h*-PdTe. Further analysis of the atomic structure models shows that the lateral crystal facets of *r*-Pd<sub>20</sub>Te<sub>7</sub> HNPs and the heterointerface exhibit angles of 30°, 90°, and 120°, corresponding to the (210), (3̄20), and (1̄30), respectively (**Figure S15**). In contrast, the analysis of *h*-PdTe HNPs indicates that the crystal facets are primarily {003} (**Figure S16**). Additionally, PdTe-PdBi HNPs also exhibit a dual-phase grain structure, where each grain contains both *h*-PdTe (**Figure 2e**) and *h*-PdBi (**Figure 2f**), with a coherent interface between the two phases, namely [001] (1̄20) of *h*-PdTe // [001] (1̄20) of *h*-PdBi, as shown in **Figures 2d** and **S17**. The atomic arrangements clearly show that the ordered Pd–Te lattice is present on the upper region of **Figure 2d** and the Pd–Bi lattice is present on the lower region, further verifying that the crystal facets of the *h*-PdBi HNPs correspond to the {003} facets (**Figure S18**). Finally, the atomic-resolution image of *h*-PdBi HNPs (**Figure 2g**), recorded along the [001] direction and corresponding FFT pattern (red inset in **Figure 2g**), confirms the single-crystalline nature. The corresponding intensity line profiles further reveal a well-ordered Pd–Bi atomic arrangement, and the measured distance between adjacent Pd atoms (0.751 nm, **Figure S19**) matches the standard lattice spacing of (1̄20) plane perpendicular to (001), confirming a perfect atomic replacement.

Based on the detailed characterization above, the overall phase transitions from *r*-Pd<sub>20</sub>Te<sub>7</sub> to *h*-PdBi are illustrated schematically in **Figure 2h,i**. The *r*-Pd<sub>20</sub>Te<sub>7</sub> is an intermetallic compound rather than an ionic telluride, as evidenced by X-ray Photoelectron Spectroscopy (XPS, **Figure S20**), which indicates that the Te species exhibit a metallic state. Thus, during the atomic replacement process, Te atoms do not serve as an anionic sublattice but exhibit higher mobility than Pd atoms, undergoing spontaneous rearrangement and substitution by Bi atoms. It was found that Te atoms could enter the *r*-Pd<sub>20</sub>Te<sub>7</sub> lattice, and HNPs subsequently transform into the *h*-PdTe phase. As shown in **Figure S21**, upon further introduction of Te atoms, *r*-Pd<sub>20</sub>Te<sub>7</sub> HNPs directly transform into *h*-PdTe HNPs without undergoing other intermediate phases, while the morphology remains unchanged. Without additional introduction of atoms under the same two-step conditions, the parent *r*-Pd<sub>20</sub>Te<sub>7</sub> HNPs undergo no phase change except for slight enlargement and thickening (**Figure S22**), further demonstrating that the additional introduction of atoms can induce the occurrence of the phase rearrangement. According to the atomic model of *r*-Pd<sub>20</sub>Te<sub>7</sub>, the Te atomic layers are arranged along the *c*-axis and separated from the Pd layers, exhibiting a stacking configuration analogous to that

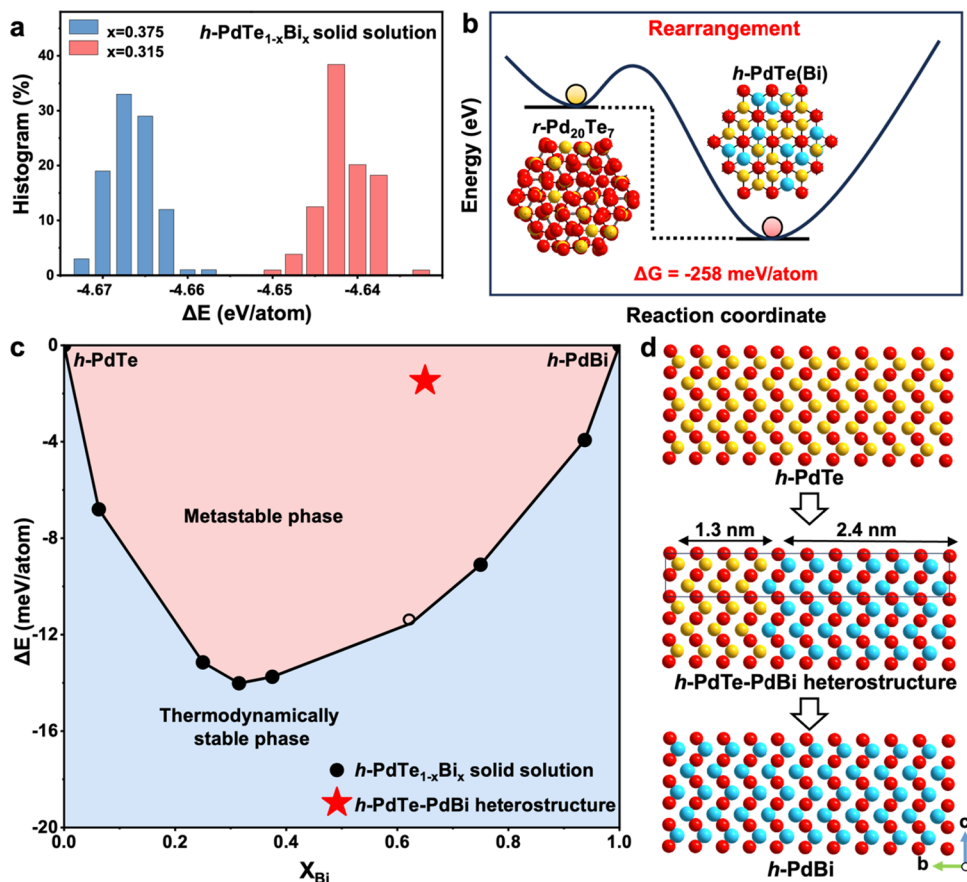


**Figure 3.** Mechanism for transformation from  $r\text{-Pd}_{20}\text{Te}_7$  to  $h\text{-PdBi}$  HNPs via atomic replacement. (a) The energy distribution of solid solutions  $\text{PdTe}_{0.625}\text{Bi}_{0.375}$  and  $\text{PdTe}_{0.685}\text{Bi}_{0.315}$ . (b) Density functional theory-calculated energy profile of the transformation from  $r\text{-Pd}_{20}\text{Te}_7$  to  $h\text{-PdTe(Bi)}$  solid solutions, verifying that phase rearrangement is prone to occur during atomic replacement. (c) Convex hull phase diagram illustrating the formation energy changes during the transformation from  $h\text{-PdTe}$  to  $h\text{-PdBi}$ . (d) Atomic schematic structural evolution of  $r\text{-Pd}_{20}\text{Te}_7$  HNPs transformation to  $h\text{-PdBi}$  HNPs via the formation of intermediate states of the  $h\text{-PdTe-PdBi}$  heterostructure along the [100] direction of the hexagonal lattice. The red, yellow, and cyan balls represent Pd, Te, and Bi atoms.

found for the Te layers in  $h\text{-PdTe}$ . The  $r\text{-Pd}_{20}\text{Te}_7$  structure is composed of hexagonally packed Te atomic layers (left side of Figure 2h), following an ABCABC… stacking sequence along the [001] axis. The  $h\text{-PdTe}$  phase has similar hexagonally packed Te atomic layers (right side of Figure 2h), but with a zigzag ABABAB… stacking pattern along the [001] axis. Transition from  $r\text{-Pd}_{20}\text{Te}_7$  to  $h\text{-PdTe}$  through the sliding of A, B, and C layers along the [1̄20] direction within the  $r\text{-Pd}_{20}\text{Te}_7$  lattice is unusual but possible (Figure 2h). The lattice volume per Te atom decreases by 3.71% in length and 12.73% in height from  $r\text{-Pd}_{20}\text{Te}_7$  to  $h\text{-PdTe}$  in the phase rearrangement. Such a pronounced change in lattice volume likely facilitates substantial mobility of the Te atoms, thereby enabling the system to rearrange into a more thermodynamically stable structure. Specifically, the  $r\text{-Pd}_{20}\text{Te}_7$  (001) facets slide along the [1̄20] crystal axis, thereby transforming into  $h\text{-PdTe}$  (001) facets, and the  $r\text{-Pd}_{20}\text{Te}_7$  (3̄20) side facets slide along the [1̄20] crystal axis to transform into the  $h\text{-PdTe}$  (300) side facets. To further understand why the replacement preferentially initiates from the side facets, we computed the adsorption energies of Bi atoms on the (3̄20) side facets and the (001) basal planes. The results show that Bi atoms exhibit significantly stronger adsorption on the (3̄20) side facets than on the (001) basal planes. This preferential adsorption facilitates nucleation and accelerates replacement along the

lateral crystal facets, thereby explaining the side-initiated anisotropic growth (Figure S23). Both  $h\text{-PdTe}$  and  $h\text{-PdBi}$  have similar crystal structures, which facilitate atomic replacement with optimal lattice matching and minimal strain. The  $h\text{-PdTe}$  phase can be indexed to the hexagonal space group  $P6_3/mmc$ , with lattice parameters  $a = b = 4.212$  and  $c = 5.75 \text{ \AA}$ . The  $h\text{-PdBi}$  phase adopts the same space group but exhibits slightly larger crystal parameters of  $a = b = 4.307$  and  $c = 5.80 \text{ \AA}$ . The volume change percent in length and height is calculated to expand by 1.66% and decrease by 0.70% during atomic replacement reactions (Figure 2i). Therefore, the total length and height volume percent changes from  $r\text{-Pd}_{20}\text{Te}_7$  to  $h\text{-PdBi}$  correspond to decreases of 2.0% and 13.42%, respectively, in agreement with the experimental statistics (Figure S24). Phase rearrangement can relieve atomic-replacement interfacial strains,<sup>28</sup> thus permitting atomic replacement to proceed despite large lattice mismatches and maintain the original morphology.

**Mechanism for Transformation from  $r\text{-Pd}_{20}\text{Te}_7$  to  $h\text{-PdBi}$  HNPs via Atomic Replacement.** First-principles calculations were carried out to elucidate the thermodynamic factors governing atomic replacement. We computed the energy change in the phase transformation from the  $r\text{-Pd}_{20}\text{Te}_7$  to the  $h\text{-PdTe}_{1-x}\text{Bi}_x$  solid solution phase by considering the following reaction:

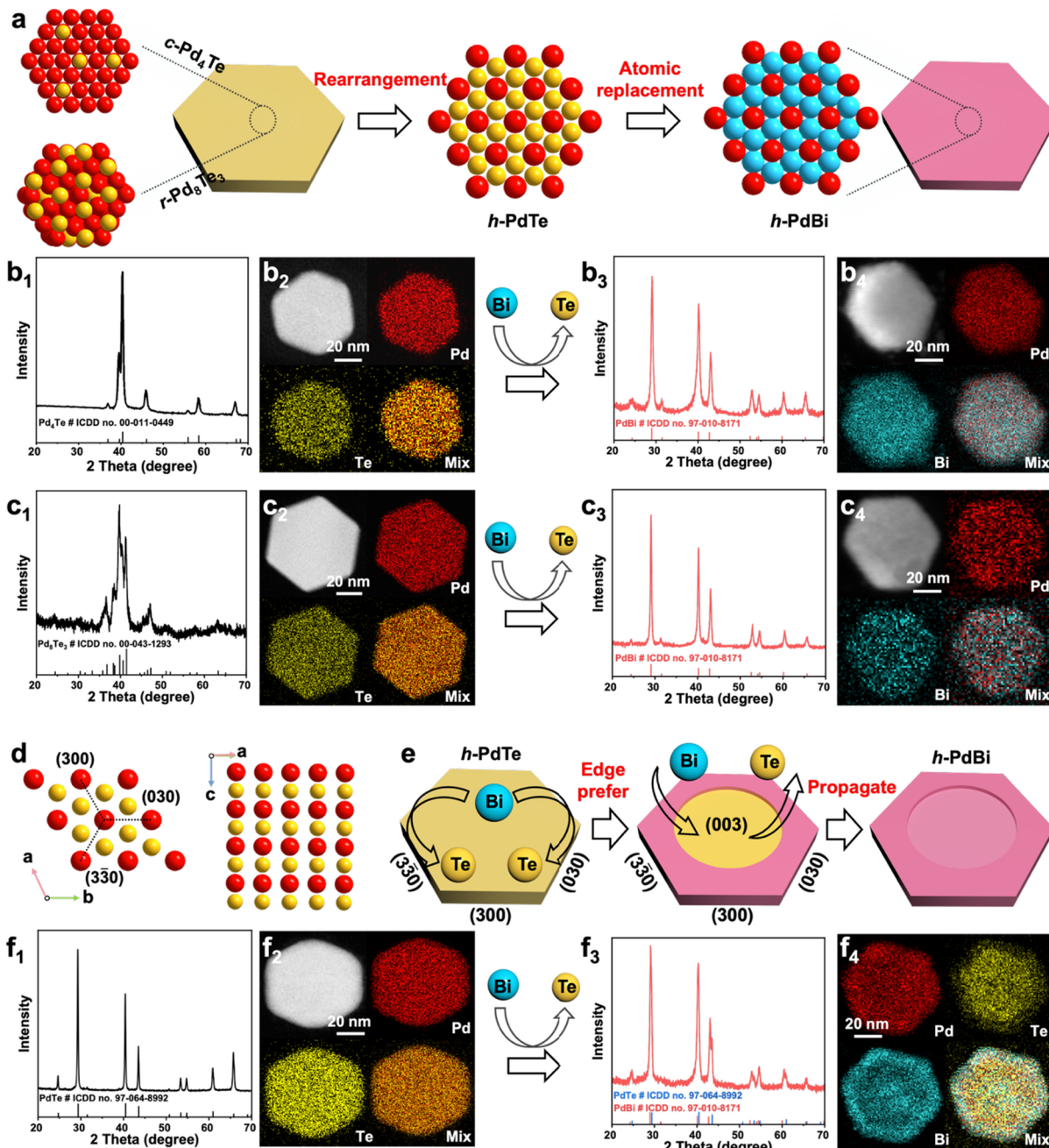
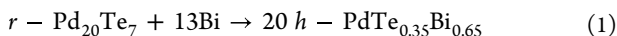


**Figure 4.** Atomic replacement for transformation from Pd–Te HNPs with different phases to *h*-PdBi. (a) Schematic structural evolution of complete transformation from *c*-Pd<sub>4</sub>Te HNPs or *r*-Pd<sub>8</sub>Te<sub>3</sub> HNPs to *h*-PdBi HNPs. (b<sub>1</sub>) XRD pattern, and (b<sub>2</sub>) elemental mapping of *c*-Pd<sub>4</sub>Te HNPs, (b<sub>3</sub>) XRD pattern, and (b<sub>4</sub>) elemental mapping of the *h*-PdBi HNPs after the transformation from *c*-Pd<sub>4</sub>Te HNPs. (c<sub>1</sub>) XRD pattern, and (c<sub>2</sub>) elemental mapping of *r*-Pd<sub>8</sub>Te<sub>3</sub> HNPs, (c<sub>3</sub>) XRD pattern, and (c<sub>4</sub>) elemental mapping of the *h*-PdBi HNPs after the transformation from *r*-Pd<sub>8</sub>Te<sub>3</sub> HNPs. (d) Crystal structure model of *h*-PdTe. (e) Schematic structural evolution of the incomplete transformation from *h*-PdTe HNPs to *h*-PdBi HNPs. (f<sub>1</sub>) XRD pattern, and (f<sub>2</sub>) elemental mapping of *h*-PdTe HNPs, (f<sub>3</sub>) XRD pattern, and (f<sub>4</sub>) elemental mapping of the *h*-PdBi HNPs after the incomplete transformation from *h*-PdTe HNPs. The red, yellow, and cyan balls represent Pd, Te, and Bi atoms.



The stoichiometric ratio in eq 1 was derived based on elemental conservation, as detailed in the Experimental Section in the Supporting Information. To calculate the energy for *h*-PdTe<sub>1-x</sub>Bi<sub>x</sub>, 100 crystal structures were generated with Te sites randomly occupied by Bi in the 2 × 2 × 2 supercell of the *h*-PdTe hexagonal lattice. Two compositions with x<sub>Bi</sub> = 0.375 and x<sub>Bi</sub> = 0.315 were investigated. The energy distributions of these solid solutions are listed in Figure 3a. Using the

Boltzmann-weighted energies of *h*-PdTe<sub>0.625</sub>Bi<sub>0.375</sub> and *h*-PdTe<sub>0.685</sub>Bi<sub>0.315</sub>, we found that the formation energy of *h*-PdTe<sub>0.35</sub>Bi<sub>0.65</sub> in reaction 1 was -258 meV/atom. This suggests that incorporating Bi atoms in the lattice and forming the *h*-PdTe<sub>1-x</sub>Bi<sub>x</sub> mixture is thermodynamically more favorable than the *r*-Pd<sub>20</sub>Te<sub>7</sub> phase, as corroborated by the observation of an intermediate *h*-PdTe<sub>1-x</sub>Bi<sub>x</sub> phase at the Pd/Bi<sub>2</sub>Te<sub>3</sub> interface.<sup>29</sup> Moreover, Bader charge analysis and electron localization function (ELF) calculations confirm that both *r*-Pd<sub>20</sub>Te<sub>7</sub> and *h*-PdTe<sub>0.35</sub>Bi<sub>0.65</sub> are metallic and charge-balanced systems (Figure

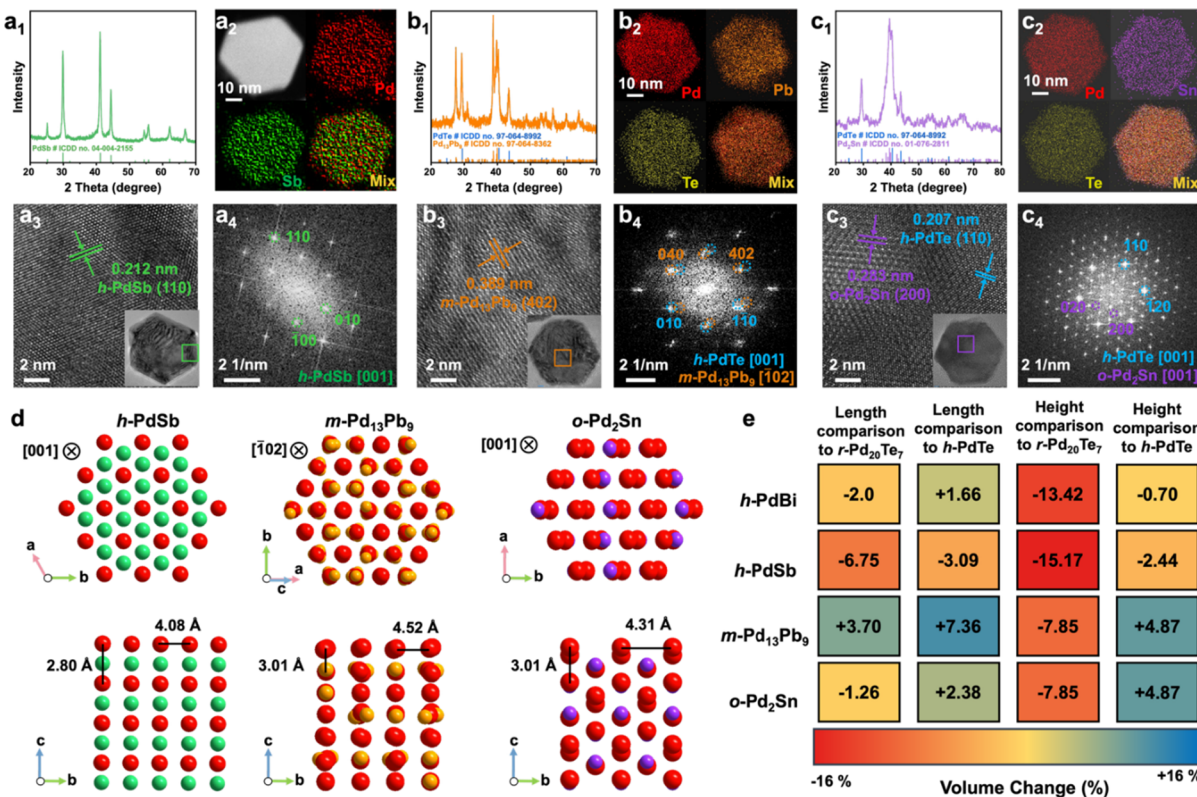
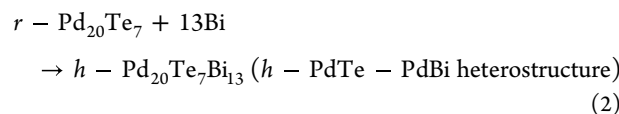


**Figure 5.** Synthesis of other intermetallics via atomic replacement. (a) Characterizations of *r*-Pd<sub>20</sub>Te<sub>7</sub> HNPs after reacting with Sb atoms: (a<sub>1</sub>) XRD pattern, (a<sub>2</sub>) elemental mapping, (a<sub>3</sub>) HRTEM image, and (a<sub>4</sub>) corresponding FFT image of *h*-PdSb HNPs. (b) Characterizations of *r*-Pd<sub>20</sub>Te<sub>7</sub> HNPs after reacting with Pb atoms. (c) Characterizations of *r*-Pd<sub>20</sub>Te<sub>7</sub> HNPs after reacting with Sn atoms. (d) Crystal structure model of *h*-PdSb, *m*-Pd<sub>13</sub>Pb<sub>9</sub>, and *o*-Pd<sub>2</sub>Sn. The red, yellow, green, orange, and purple balls represent Pd, Te, Sb, Pb, and Sn atoms. (e) Heat map of the lattice mismatch percentage, reflecting the interfacial strain generated during phase rearrangement and atomic replacement when *r*-Pd<sub>20</sub>Te<sub>7</sub> HNPs react with four different metal atoms along the observed crystallographic orientation. The color scale indicates the degree of lattice-spacing variation: yellow corresponds to a small lattice mismatch (low strain), whereas blue and red denote large lattice mismatches associated with expansion strain and compressive strain, respectively.

S25). This indicates that phase rearrangements from the rhombohedral to the hexagonal phases are likely to occur (Figure 3b). Such a tendency largely arises from the relatively weak M–Te bonds, which are noticeably much weaker than the corresponding M–S and M–Se bonds.<sup>30,31</sup> The lower rigidity of the tellurium lattice results in a greater tendency to deform or dissolve under similar template conditions. Therefore, in Te-related template methods, the entire crystal may become mobile under nonequilibrium conditions, inducing phase rearrangements that lead to the formation of thermodynamically more stable structures.<sup>32</sup>

To further investigate the possibility of atomic replacement occurring from *h*-PdTe to *h*-PdBi, we evaluated the stability using a convex hull phase diagram of the *h*-PdTe<sub>1-x</sub>Bi<sub>x</sub> solid solution (Figure 3c). At any given composition, numerous hypothetical nonground-state polymorphs may exist. In the diagram, the solid line denotes the convex hull. Points that lie on this line (black circles) or at the bottom of the hull (blue regions) correspond to thermodynamically stable phases, whereas points above the hull (red regions) represent metastable phases. Therefore, the *h*-PdTe<sub>1-x</sub>Bi<sub>x</sub> solid solution is confirmed to be stable. As the amount of Bi atoms increases, more Te atoms become available for exchange, which further facilitates atomic replacement from *h*-PdTe to *h*-PdBi. Meanwhile, we also computed the energy change for the phase transformation from the *r*-Pd<sub>20</sub>Te<sub>7</sub> phase to the

heterostructure between *h*-PdTe and *h*-PdBi by considering the following reaction:



The Pd<sub>20</sub>Te<sub>7</sub>Bi<sub>13</sub> (*h*-PdTe-PdBi heterostructure) was constructed with a hexagonal cell oriented along the [100] direction (Figure 3d). The calculations show that the energy decreases by 222 meV/atom in this reaction (Figure S26). This suggests that the incorporation of Bi into the hexagonal lattice and the formation of the *h*-PdTe-PdBi heterostructure is thermodynamically more favorable than the *r*-Pd<sub>20</sub>Te<sub>7</sub> phase. Compared with the *h*-PdTe<sub>1-x</sub>Bi<sub>x</sub> solid solutions phase diagram above, the energy of *h*-PdTe-PdBi heterostructure is only slightly higher (~10 meV/atom) than the stable solid solution phase and close to that of *h*-PdBi, thus explaining why the intermediate states of *h*-PdTe-PdBi heterostructures are prone to forming during the *r*-Pd<sub>20</sub>Te<sub>7</sub> transition to *h*-PdBi. In contrast, although hexagonal PdTe<sub>2</sub> (*h*-PdTe<sub>2</sub>) also adopts a hexagonal lattice, our interfacial energy calculations demonstrate that PdTe<sub>2</sub>-PdBi heterostructures are thermodynamically unfavorable, further confirming that the transformation pathway preferentially proceeds through *h*-PdTe and eventually to *h*-PdBi (Figure S27).

**Atomic Replacement for the Transformation from Pd–Te HNPs with Different Phases to *h*-PdBi.** To study the effects of crystal phase during the exchange process, we synthesized a series of HNPs with different crystal phases<sup>26</sup> (from *r*-Pd<sub>20</sub>Te<sub>7</sub> to cubic phase Pd<sub>4</sub>Te (*c*-Pd<sub>4</sub>Te), rhombohedral phase Pd<sub>8</sub>Te<sub>3</sub> (*r*-Pd<sub>8</sub>Te<sub>3</sub>), and *h*-PdTe) as the sacrificial templates (Figures S28–S30). The SEM-EDS profiles display Pd:Te atomic ratios of 78.07:21.93, 70.28:29.72, and 51.03:48.97, corresponding to XRD results of *c*-Pd<sub>4</sub>Te (ICDD no. 00-011-0449) (Figure 4b<sub>1</sub>), *r*-Pd<sub>8</sub>Te<sub>3</sub> (ICDD no. 00-043-1293) (Figure 4c<sub>1</sub>), and *h*-PdTe (ICDD no. 97-064-8992) (Figure 4f<sub>1</sub>), respectively, which are consistent with the inductively coupled plasma optical emission spectrometer (ICP-OES) results. TEM characterization of *c*-Pd<sub>4</sub>Te, *r*-Pd<sub>8</sub>Te<sub>3</sub>, and *h*-PdTe HNPs reveals well-defined HNP morphologies, with average lengths of 58.0, 70.0, and 65.0 nm and heights of 19.7, 17.2, and 18.3 nm, respectively. Element mapping analyses of *c*-Pd<sub>4</sub>Te HNPs (Figure 4b<sub>2</sub>), *r*-Pd<sub>8</sub>Te<sub>3</sub> HNPs (Figure 4c<sub>2</sub>), and *h*-PdTe HNPs (Figure 4f<sub>2</sub>) suggest homogeneous distributions of Pd and Te in the HNPs. Subsequently, we added excessive Bi atoms to the Pd–Te templates for the atomic replacement. A similar atomic replacement mechanism with *r*-Pd<sub>20</sub>Te<sub>7</sub> is observed in *c*-Pd<sub>4</sub>Te and *r*-Pd<sub>8</sub>Te<sub>3</sub>, as shown in Figure 4a, indicating that they all undergo phase rearrangement to a thermodynamically more stable phase *h*-PdTe, and then are transformed via atomic replacement into *h*-PdBi. Partially reacted *c*-Pd<sub>4</sub>Te HNPs exhibit the coexistence of the *c*-Pd<sub>4</sub>Te phase (ICDD no. 00-011-0449) and *h*-PdTe (ICDD no. 97-064-8992), confirming that the phase rearrangement from *c*-Pd<sub>4</sub>Te to *h*-PdTe occurs before atomic replacement (Figure S31). With the further addition of Bi atoms, *c*-Pd<sub>4</sub>Te fully transforms into *h*-PdBi (ICDD no. 97-010-8171), as shown in Figure 4b<sub>3</sub>. The STEM elemental mapping (Figure 4b<sub>4</sub>) indicates homogeneous distributions of Pd and Bi within the HNPs, and the Pd:Bi atomic ratio is estimated to be approximately 1:1. The *c*-Pd<sub>4</sub>Te HNPs morphology does not change after atomic replacement (Figure S32). Analogous results are also obtained in the atomic replacement between *r*-Pd<sub>8</sub>Te<sub>3</sub> and Bi atoms (Figures 4c, S33, and S34). Interestingly, using *h*-PdTe HNPs as parent templates, *h*-PdTe and *h*-PdBi have similar atomic arrangement on the (003), (300), (030), and (3̄30) crystal facets (Figure 4d). From the [001] direction, Pd and Te layers are alternately stacked, allowing Te atoms to move freely within the intralayer channels for atomic replacement. The preferential exchange occurs on the lateral facets of the *h*-PdTe HNPs, driven by optimal lattice matching and minimal strain (Figure 4e). However, the atomic replacement reaction is incomplete due to the Kirkendall effect (Figure S35), which involves an imbalance between the diffusivity of outgoing Te atoms ( $D_{Te}$ ) and incoming Bi atoms ( $D_{Bi}$ ), with  $D_{Te} \gg D_{Bi}$ .<sup>33</sup> The XRD patterns show the coexistence of the *h*-PdTe phase (ICDD no. 97-064-8992) and *h*-PdBi (ICDD no. 97-004-2552) (Figure 4f<sub>3</sub>). Elemental mapping further shows that Bi atoms are primarily located at the edges of the HNPs (Figure 4f<sub>4</sub>), whereas Te atoms remain concentrated in the center. Unlike the earlier Pd–Te systems that undergo full exchange with Bi, here the Bi atoms preferentially react along the lateral facets containing layered Te channels, owing to optimal lattice matching and minimal strain.<sup>34</sup> In addition, the large atomic radii of Bi and Te, together with the relatively large particle size of the HNPs, hinder the diffusion of Te atoms from the interior, resulting in residual Te remaining at the center.

**Synthesis of Other intermetallics via Atomic Replacement.** Based on this emerging design criterion, as well as a deep understanding of formation processes during atomic replacement, *r*-Pd<sub>20</sub>Te<sub>7</sub> HNPs were used as parent templates to exchange with three other metallic atoms (Sb, Pb, and Sn). Sb atoms can form a highly crystalline hexagonal phase PdSb (*h*-PdSb), similar to *h*-PdTe via complete atomic replacement (Figure 5a<sub>1</sub>), while Pb and Sn atoms tend to form a monoclinic phase Pd<sub>13</sub>Pb<sub>9</sub> (*m*-Pd<sub>13</sub>Pb<sub>9</sub>) (Figure 5b<sub>1</sub>) and an orthorhombic phase Pd<sub>2</sub>Sn (*o*-Pd<sub>2</sub>Sn) (Figure 5c<sub>1</sub>), respectively. The element mapping analysis (Figure 5a<sub>2</sub>) and line scan results (Figure S36) of *h*-PdSb HNPs show that Pd (red) and Sb (green) are distributed homogeneously throughout the HNPs without noticeable compositional segregation. Regarding atomic replacement of *r*-Pd<sub>20</sub>Te<sub>7</sub> HNPs with Sb atoms, a single *h*-PdSb (ICDD no. 04-004-2155) was detected. In the HRTEM image of the *h*-PdSb HNPs (Figure 5a<sub>3</sub>), distinct lattice fringes with a 0.212 nm spacing are observed, consistent with the (110) planes of *h*-PdSb. The corresponding FFT pattern (Figure 5a<sub>4</sub>) displays a p6-symmetric pattern that can be indexed to the [001] crystal axis. These results confirm the atomic replacement reaction between *r*-Pd<sub>20</sub>Te<sub>7</sub> HNPs and Sb atoms, analogous to that with Bi atoms, ultimately leading to a single-crystalline phase of *h*-PdSb similar to those of *h*-PdTe and *h*-PdBi. For the exchange between *r*-Pd<sub>20</sub>Te<sub>7</sub> HNPs and Pb atoms, a phase rearrangement also occurs. Unlike the atomic replacement with Bi and Sb atoms mentioned above, *m*-Pd<sub>13</sub>Pb<sub>9</sub> (ICDD no. 97-064-8362) is identified as the main product (Figure 5b<sub>1</sub>), along with the coexisting *h*-PdTe phase (named PdTe-Pd<sub>13</sub>Pb<sub>9</sub> HNPs). The element mapping analysis (Figure 5b<sub>2</sub>) and line-scan profiles (Figure S37) show that Pd (red) and Pb (orange) exhibit strong signals and are uniformly distributed across the whole HNPs. The HRTEM image (Figure 5b<sub>3</sub>) displays lattice fringes of 0.389 nm belonging to the *m*-Pd<sub>13</sub>Pb<sub>9</sub> (402) facets or the *h*-PdTe (010) facets, which are too close to be distinguished. The corresponding FFT image (Figure 5b<sub>4</sub>) shows two sets of diffraction spots indexed to the [102] region axis of *m*-Pd<sub>13</sub>Pb<sub>9</sub> and the [001] region axis of *h*-PdTe, respectively, supporting the formation of a heterogeneous structure with two coexisting phases. Further analysis of *r*-Pd<sub>20</sub>Te<sub>7</sub> HNPs reacting with Sn atoms via atomic replacement shows that the *h*-PdTe phase and *o*-Pd<sub>2</sub>Sn (ICDD no. 01-076-2811) coexist (Figure 5c<sub>1</sub>), namely PdTe-Pd<sub>2</sub>Sn HNPs. Element mapping analysis (Figure 5c<sub>2</sub>) and line-scan profiles (Figure S38) of PdTe-Pd<sub>2</sub>Sn HNPs demonstrate that Pd, Te, and Sn are evenly distributed across the HNPs, indicating that the atomic replacement reaction occurs between *r*-Pd<sub>20</sub>Te<sub>7</sub> HNPs and Sn atoms. As shown in Figure 5c<sub>3</sub>, there are obvious grain boundaries and two different lattice spacings, specifically 0.283 nm corresponding to *o*-Pd<sub>2</sub>Sn (200) facets and 0.207 nm corresponding to *h*-PdTe (110) facets, respectively. The corresponding FFT image (Figure 5c<sub>4</sub>) shows two sets of diffraction spots corresponding to the [001] region axis of *o*-Pd<sub>2</sub>Sn and the [001] region axis of *h*-PdTe, further supporting the coexistence of two phases. It is worth mentioning that incomplete phase transitions between Pb/Sn atoms and *r*-Pd<sub>20</sub>Te<sub>7</sub> HNPs can be attributed to the absence of hexagonal-phase alloys similar to those of *h*-PdBi in Pd–Pb and Pd–Sn systems. The introduction of Pb and Sn atoms into the *r*-Pd<sub>20</sub>Te<sub>7</sub> lattice occupies some vacancies, leading to a lattice transition toward the *h*-PdTe phase.

To further understand why different architectures and interfaces within the *r*-Pd<sub>20</sub>Te<sub>7</sub> HNP library exhibit distinct

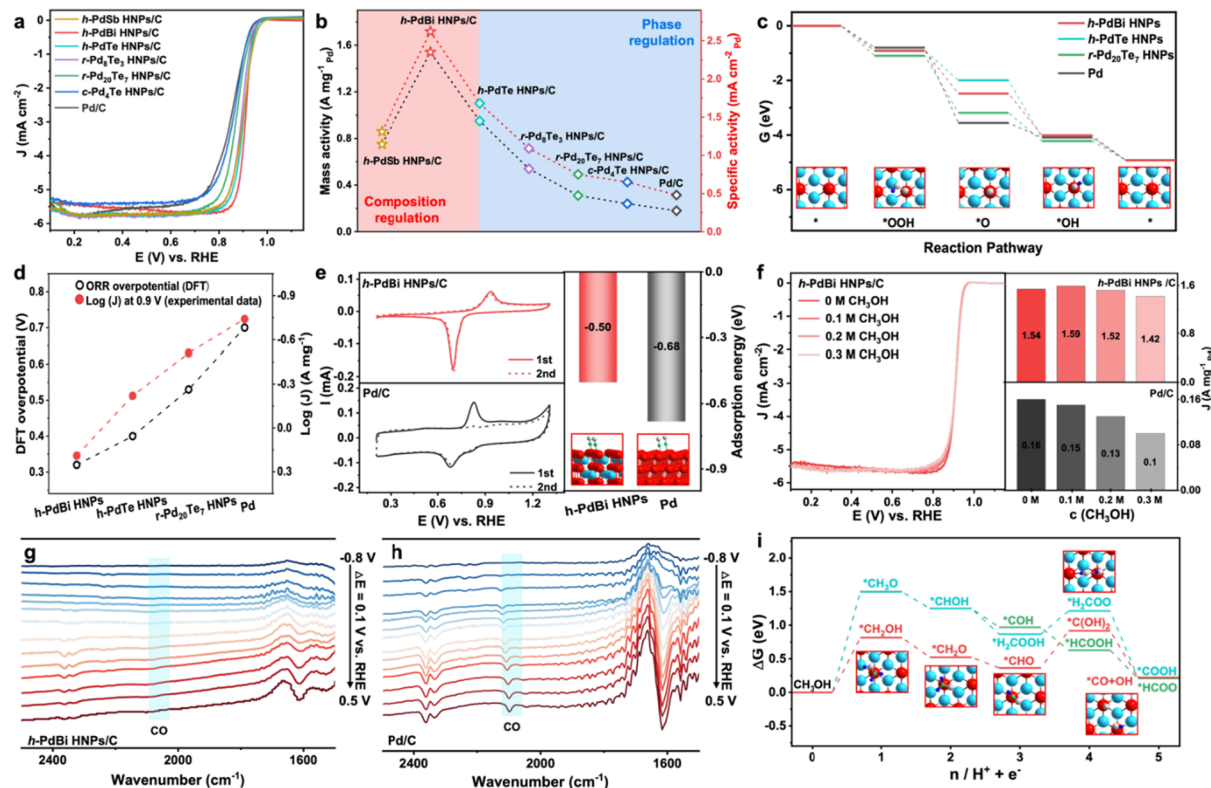


**Figure 6.** Electrocatalytic performance study toward ORR and antipoisoning methanol capability. (a) ORR polarization curves measured in  $O_2$ -saturated 0.1 M KOH at a scan rate of  $10\text{ mV s}^{-1}$  and a rotation speed of 1600 rpm, and (b) comparison of the mass activity and the ECSA-normalized specific activity at 0.9 V vs RHE for different catalysts. (c) ORR reaction pathways, and the insets are optimized structures of the key intermediates on *h*-PdBi HNPs. (d) DFT-calculated overpotentials under standard conditions and RDE current density recorded at 0.9 V vs RHE for the ORR. (e) CO-stripping curves of *h*-PdBi HNPs/C and Pd/C recorded in  $N_2$ -saturated 0.1 M KOH (left) and comparison of CO adsorption energies (right). (f) The response of *h*-PdBi HNPs/C at different  $CH_3OH$  concentrations in  $O_2$ -saturated 0.1 M KOH (left), and corresponding mass activities at 0.9 V vs RHE at different  $CH_3OH$  concentrations of *h*-PdBi HNPs/C and Pd/C. In situ ATR-SEIRAS varied from  $-0.8$  to  $0.2\text{ V}$  vs RHE in 0.1 M KOH + 0.3 M  $CH_3OH$  of (g) *h*-PdBi HNPs/C and (h) Pd/C. (i) Calculated free-energy profiles of possible MOR intermediates on *h*-PdBi HNPs. The most stable intermediates for each step are shown in red, and the inset shows the optimized structures of the most stable intermediates for MOR.

reactivity toward metal atoms, we compared the crystal phases of *h*-PdSb, *m*-Pd<sub>13</sub>Pb<sub>9</sub>, and *o*-Pd<sub>2</sub>Sn using the aforementioned characterization results to elucidate their lattice-matching relationships (Figure 5d). All three phases exhibit comparable structural motifs, consisting of hexagonally close-packed atomic layers oriented along specific directions with a layered arrangement along the *c*-axis that facilitates atomic replacement. The hexagonal close-packed lattice parameters of *h*-PdSb (4.08 Å), *m*-Pd<sub>13</sub>Pb<sub>9</sub> (4.52 Å), and *o*-Pd<sub>2</sub>Sn (4.31 Å) are similar to *r*-Pd<sub>20</sub>Te<sub>7</sub> (4.47 Å) and *h*-PdTe (4.21 Å) (Table S2), whereas the *c*-axis lattice parameters of *h*-PdSb (2.80 Å), *m*-Pd<sub>13</sub>Pb<sub>9</sub> (3.01 Å), and *o*-Pd<sub>2</sub>Sn (3.01 Å) are similar to *h*-PdTe (2.87 Å) but differ substantially from *r*-Pd<sub>20</sub>Te<sub>7</sub> (4.40 Å). Figure 5e shows a heat map corresponding to the lattice mismatch percentages, which represents the interfacial strain arising during phase rearrangement and atomic replacement for *r*-Pd<sub>20</sub>Te<sub>7</sub> HNPs reacting with four different metal atoms along the observed crystallographic orientations.<sup>35</sup> Here, yellow means small lattice mismatch and low strain, while blue means high expansion strain, and red color means high compressive strain, both indicating large lattice mismatch. Overall, during this reaction, the phase rearrangement process initially experiences large strains, especially at the height where large compressive strains exist. Thus, this phase rearrangement from the metastable *r*-Pd<sub>20</sub>Te<sub>7</sub> HNPs to thermodynamically

more stable *h*-PdTe HNPs significantly relieves the strain arising from the atomic replacement reaction, thereby facilitating the subsequent replacement process. Meanwhile, the experimentally determined lattice strains of the four atomic replacement products, referenced to their parent templates, were measured to be  $-6.75$  and  $15.17\%$  of *h*-PdSb HNPs,  $+3.70$  and  $-7.85\%$  of PdTe-Pd<sub>13</sub>Pb<sub>9</sub>,  $-1.26$  and  $-7.85\%$  of PdTe-Pd<sub>2</sub>Sn (Figures S39–S41) and Table S3. These values align well with the lattice-mismatch trends predicted from atomic-model calculations. These results confirm that crystal transitions with smaller lattice mismatch values are favored, which explains why Sb and Bi atoms undergo more complete exchange due to better matching of their structural parameters with *h*-PdTe HNPs.

**Electrocatalytic ORR Performance and Antipoisoning Methanol Capability.** To validate the potential effect of different phases and composition catalysts on performance, we selected Pd–Te HNPs/C with different phases (Figure S42) and *h*-PdM HNPs/C with different compositions (*M* = Te, Bi, Sb, Figure S43) as representative catalysts, while commercial Pd/C (Figure S44) was chosen for comparison. The ORR performance was assessed by rotating disk electrode (RDE) measurements in  $O_2$ -saturated 0.1 M KOH electrolyte, and all potentials were referenced to the reversible hydrogen electrode (RHE) (Figure 6a). The electrochemically active surface areas

(ECSAs) determined for *h*-PdSb, *h*-PdBi, *h*-PdTe, *r*-Pd<sub>8</sub>Te<sub>3</sub>, *r*-Pd<sub>20</sub>Te<sub>7</sub>, *c*-Pd<sub>4</sub>Te HNPs/C, and commercial Pd/C were 57.1, 58.6, 56.3, 49.2, 41.2, 36.8, and 37.6 mA cm<sub>Pd</sub><sup>-2</sup>, respectively (Figure S45). Among the Pd–Te HNPs/C with different phases, the *h*-PdTe HNPs/C displayed a remarkable mass activity (MA) of 0.95 A mg<sub>Pd</sub><sup>-1</sup> and specific activity (SA) of 1.68 mA cm<sub>Pd</sub><sup>-2</sup> (Figure 6b and Table S4), surpassing all other Pd–Te HNPs/C and commercial Pd/C, indicating that hexagonal Pd-based phases are intrinsically more active toward ORR. We then compared catalysts with the same hexagonal phase but different compositions, where *h*-PdBi HNPs/C exhibited the highest MA of 1.54 A mg<sub>Pd</sub><sup>-1</sup> and SA of 2.62 mA cm<sub>Pd</sub><sup>-2</sup>, exceeding those of *h*-PdSb HNPs/C (MA of 0.75 A mg<sub>Pd</sub><sup>-1</sup> and SA of 1.31 mA cm<sub>Pd</sub><sup>-2</sup>) and *h*-PdTe HNPs/C, illustrating the significant composition effect. DFT calculations were performed to elucidate the improved catalytic behavior observed for the *h*-PdBi HNPs. Based on the experimentally identified surface structures, *h*-PdBi HNPs (001) (Figure S46), *h*-PdTe HNPs (001) (Figure S47), *r*-Pd<sub>20</sub>Te<sub>7</sub> HNPs (001) (Figure S48), and Pd (111) (Figure S49) were modeled for DFT calculations. Analysis of the calculated Gibbs free energies of the reaction intermediates (Figure 6c) shows that *h*-PdBi HNPs bind \*OH more weakly than the other catalysts, which facilitates \*OH desorption in the final step and enhances the ORR kinetics. Moreover, the DFT-predicted overpotentials are consistent with the experimentally measured RDE current densities (Figure 6d and Table S5). Among all catalysts, *h*-PdBi HNPs show the lowest overpotentials and the highest current densities. Furthermore, the incorporation of Te or Sb downshifts the Pd d-band centers in *c*-Pd<sub>4</sub>Te, *r*-Pd<sub>8</sub>Te<sub>3</sub>, and *h*-PdSb, thereby weakening oxygenated intermediate binding and accounting for their enhanced ORR performance (Figure S50). Next, the stability of prepared catalysts via atomic replacement was evaluated through the accelerated durability tests (ADT), where *h*-PdBi HNPs/C exhibited negligible MA decay and partial loss of limiting current density after 20,000 ADT cycles in alkaline solution (Figure S51). TEM image, HRTEM image, and elemental mapping of *h*-PdBi HNPs/C after the ADT test showed that the morphology and structure remained intact (Figures S52 and S53).

Interestingly, *h*-PdBi HNPs/C also demonstrated excellent tolerance to CO and methanol poisoning, as confirmed by both the CO stripping and DFT calculations (Figure 6e). The CO adsorption energy on *h*-PdBi HNPs was -0.50 eV, while that on Pd was -0.68 eV, indicating superior CO tolerance for *h*-PdBi HNPs/C. The antipoisoning methanol performance of *h*-PdBi HNPs/C (Figure 6f) and Pd/C (Figure S54) was evaluated, where *h*-PdBi HNPs/C exhibited negligible current response to methanol, in contrast to the pronounced methanol oxidation peaks observed for Pd/C (Figure S55). The antipoisoning methanol behavior was further examined using in situ attenuated total reflection surface-enhanced infrared reflection absorption spectroscopy (ATR-SEIRAS). The downward bands at 2095 cm<sup>-1</sup> were attributed to the linearly absorbed CO, which was the intermediate species of CH<sub>3</sub>OH decomposition on Pd/C (Figure 6h). However, no such intermediate was detected on *h*-PdBi HNPs/C (Figure 6g). The antipoisoning methanol performance of *h*-PdBi HNPs/C was further evaluated by DFT calculations (Figure 6i). The formation energy of CH<sub>2</sub>OH\* is considerably lower than that of CH<sub>3</sub>O\*; therefore, the reaction preferentially proceeds via CH<sub>2</sub>OH\* as the initial intermediate. In particular, the rate-determining step in all possible pathways is the transformation

of CH<sub>3</sub>OH to CH<sub>2</sub>OH\* with the ΔG value of 0.815 eV on *h*-PdBi HNPs, exhibiting a relatively higher energy barrier than Pd,<sup>36</sup> which rationally explains the experimentally observed excellent antipoisoning methanol ability.

## CONCLUSIONS

A general and robust transformation strategy for greatly expanding intermetallic libraries has been demonstrated via phase-rearrangement-induced atomic replacement with previously unreported synthesis mechanisms that enable finer manipulation of extensive intermetallics and heterointerfaces. In contrast to conventional template methods, Te no longer functions as a stable anionic sublattice but instead is exchanged with other metal atoms (Bi, Sb, Pb, and Sn). Detailed analyses show that phase rearrangement to the thermodynamically more stable structure (*h*-PdTe) occurs before atomic replacement while preserving morphology, offering significant promise for further engineering and investigation of exchanges involving large lattice mismatches. Such atomic replacement methods are further supported by phase regulation, where *c*-Pd<sub>4</sub>Te, *r*-Pd<sub>20</sub>Te<sub>7</sub>, and *r*-Pd<sub>8</sub>Te<sub>3</sub> HNPs used as parent templates retain their original morphology through phase rearrangement, while *h*-PdTe HNPs used as parent templates generate voids due to the Kirkendall effect. Moreover, various morphologies of *r*-Pd<sub>20</sub>Te<sub>7</sub> (including 0D NPs, 1D NWs, and 2D HNPs) have also been successfully applied, demonstrating the generality of atomic replacement. This work provides important insights into the formation and transformation mechanism of intermetallics and will further greatly facilitate the synthesis of complex multifunctional intermetallics, demonstrating the underlying effects of different phases and compositions on catalyst performance.

## ASSOCIATED CONTENT

### Supporting Information

The Supporting Information is available free of charge at <https://pubs.acs.org/doi/10.1021/jacs.Sc16486>.

Experimental details including chemicals, synthetic procedures, materials characterization, electrochemical measurements, in situ ATR-SEIRAS measurements, and DFT computational methods; supporting figures and tables including XRD patterns, TEM and HRTEM images, SEM-EDS and ICP-OES analyses, HAADF-STEM and atomic-resolution STEM images, line-scan profiles, EDS spectra, atomic structure models, XPS spectra, ELF analyses, DFT calculation results, electrocatalytic performance data, unit-cell parameters, and strain-analysis tables (PDF)

## AUTHOR INFORMATION

### Corresponding Authors

Xian-Kui Wei – State Key Laboratory of Physical Chemistry of Solid Surfaces, College of Chemistry and Chemical Engineering, Xiamen University, Xiamen 361005, China; Innovation Laboratory for Sciences and Technologies of Energy Materials of Fujian Province (IKKEM), Xiamen 361005, China; [orcid.org/0000-0003-4320-1120](https://orcid.org/0000-0003-4320-1120); Email: [xkwei@xmu.edu.cn](mailto:xkwei@xmu.edu.cn)

Qi Shao – College of Chemistry, Chemical Engineering and Materials Science, Soochow University, Suzhou 215123, China; [orcid.org/0000-0002-9858-0458](https://orcid.org/0000-0002-9858-0458); Email: [qshao@suda.edu.cn](mailto:qshao@suda.edu.cn)

Xiaqing Huang – State Key Laboratory of Physical Chemistry of Solid Surfaces, College of Chemistry and Chemical Engineering, Xiamen University, Xiamen 361005, China; Innovation Laboratory for Sciences and Technologies of Energy Materials of Fujian Province (IKKEM), Xiamen 361005, China; [ORCID iD](https://orcid.org/0000-0003-3219-4316); Email: [hxq006@xmu.edu.cn](mailto:hxq006@xmu.edu.cn)

## Authors

Xuan Huang – State Key Laboratory of Physical Chemistry of Solid Surfaces, College of Chemistry and Chemical Engineering, Xiamen University, Xiamen 361005, China; College of Chemistry, Chemical Engineering and Materials Science, Soochow University, Suzhou 215123, China; [ORCID iD](https://orcid.org/0009-0003-1830-9663)

Bingyan Xu – State Key Laboratory of Physical Chemistry of Solid Surfaces, College of Chemistry and Chemical Engineering, Xiamen University, Xiamen 361005, China

Yang Sun – Department of Physics, Xiamen University, Xiamen 361005, China; [ORCID iD](https://orcid.org/0000-0002-4344-2920)

Zhiyao Liang – State Key Laboratory of Physical Chemistry of Solid Surfaces, College of Chemistry and Chemical Engineering, Xiamen University, Xiamen 361005, China

Changhong Zhan – State Key Laboratory of Physical Chemistry of Solid Surfaces, College of Chemistry and Chemical Engineering, Xiamen University, Xiamen 361005, China

Jiafeng Du – State Key Laboratory of Physical Chemistry of Solid Surfaces, College of Chemistry and Chemical Engineering, Xiamen University, Xiamen 361005, China

Jie Feng – Institute of Functional Nano & Soft Materials (FUNSOM), Jiangsu Key Laboratory for Carbon-Based Functional Materials & Devices, Soochow University, Suzhou, Jiangsu 215123, China

Youyong Li – Institute of Functional Nano & Soft Materials (FUNSOM), Jiangsu Key Laboratory for Carbon-Based Functional Materials & Devices, Soochow University, Suzhou, Jiangsu 215123, China; [ORCID iD](https://orcid.org/0000-0002-5248-2756)

Yujin Ji – Institute of Functional Nano & Soft Materials (FUNSOM), Jiangsu Key Laboratory for Carbon-Based Functional Materials & Devices, Soochow University, Suzhou, Jiangsu 215123, China; [ORCID iD](https://orcid.org/0000-0003-3177-2073)

Complete contact information is available at:  
<https://pubs.acs.org/10.1021/jacs.Sc16486>

## Author Contributions

#X.H., Y.X., Y.S., and Z.L. contributed equally to this work.

## Notes

The authors declare no competing financial interest.

## ACKNOWLEDGMENTS

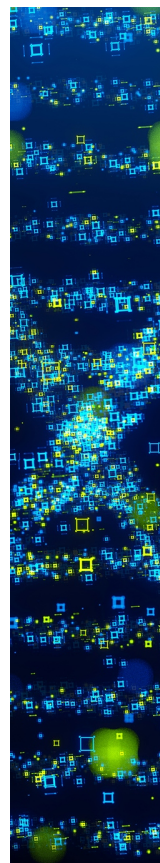
This work was financially supported by the Ministry of Science and Technology of China (2024YFA1509500), the National Key R&D Program of China (2022YFA1504500), the National Natural Science Foundation of China (22025108, U21A20327, 22121001, 224B2508, T2422016, 22475143), the Fundamental Research Funds for the Central Universities (20720240059, 20720240053, 20720230014), the start-up funding from Xiamen University, the Postdoctoral Fellowship Program of

CPSF (GZB20240393), the National High-Level Youth Talents Program (Grant Nos. 0040/X2450224, 0040/K2923004), the Xiamen Natural Science Foundation Program (Grant No. 3502Z202573024), the Xiamen University President's Fund Program (Grant No. 20720230006), the State Key Laboratory of Vaccines for Infectious Diseases of Xiang An Biomedicine Laboratory (Grant No. 2024XAKJ0100006), and the Jiangsu Natural Science Fund for Distinguished Young Scholars (BK20250047), Young Elite Scientists Sponsorship Program by CAST (grant no. 2023QNRC001), the Priority Academic Program Development of Jiangsu Higher Education Institutions (PAPD) and Collaborative Innovation Center of Suzhou Nano Science and Technology.

## REFERENCES

- (1) Amato, I. Exploring the New Material World. *Science* **1991**, *252*, 644–646.
- (2) Zhou, M.; Li, C.; Fang, J. Noble-Metal Based Random Alloy and Intermetallic Nanocrystals: Syntheses and Applications. *Chem. Rev.* **2021**, *117*, 736–795.
- (3) Shi, Y.; Lyu, Z.; Zhao, M.; Chen, R.; Nguyen, Q. N.; Xia, Y. Noble-Metal Nanocrystals with Controlled Shapes for Catalytic and Electrocatalytic Applications. *Chem. Rev.* **2021**, *121*, 649–735.
- (4) Nguyen, Q. N.; Wang, C.; Shang, Y.; Janssen, A.; Xia, Y. Colloidal Synthesis of Metal Nanocrystals: From Asymmetrical Growth to Symmetry Breaking. *Chem. Rev.* **2023**, *123*, 3693–3760.
- (5) Xie, C.; Niu, Z.; Kim, D.; Li, M.; Yang, P. Surface and Interface Control in Nanoparticle Catalysis. *Chem. Rev.* **2020**, *120*, 1184–1249.
- (6) Swisher, J. H.; Jibril, L.; Petrosko, S. H.; Mirkin, C. A. Nanoreactors for Particle Synthesis. *Nat. Rev. Mater.* **2022**, *7*, 428–448.
- (7) Pearce, A. K.; Wilks, T. R.; Arno, M. C.; O'Reilly, R. K. Synthesis and Applications of Anisotropic Nanoparticles with Precisely Defined Dimensions. *Nat. Rev. Chem.* **2021**, *5*, 21–45.
- (8) He, T.; Wang, W.; Shi, F.; Yang, X.; Li, X.; Wu, J.; Yin, Y.; Jin, M. Mastering the Surface Strain of Platinum Catalysts for Efficient Electrocatalysis. *Nature* **2021**, *598*, 76–81.
- (9) Loijudice, A.; Buonsanti, R. Reaction Intermediates in the Synthesis of Colloidal Nanocrystals. *Nat. Synth.* **2022**, *1*, 344–351.
- (10) Lohse, S. E.; Burrows, N. D.; Scarabelli, L.; Liz-Marzán, L. M.; Murphy, C. J. Anisotropic Noble Metal Nanocrystal Growth: the Role of Halides. *Chem. Mater.* **2014**, *26*, 34–43.
- (11) Langille, M. R.; Personick, M. L.; Zhang, J.; Mirkin, C. A. Defining Rules for the Shape Evolution of Gold Nanoparticles. *J. Am. Chem. Soc.* **2012**, *134*, 14542–14554.
- (12) Huang, L.; Liu, M.; Lin, H.; Xu, Y.; Wu, J.; Dravid, V. P.; Wolverton, C.; Mirkin, C. A. Shape Regulation of High-Index Facet Nanoparticles by Dealloying. *Science* **2019**, *365*, 1159–1163.
- (13) Han, M.; Kani, K.; Na, J.; Kim, J.; Bando, Y.; Ahamed, T.; Alshehri, S. M.; Yamauchi, Y. Retrospect and Prospect: Nanoarchitectonics of Platinum-Group-Metal-Based materials. *Adv. Funct. Mater.* **2023**, *33*, No. 2301831.
- (14) Gilroy, K. D.; Ruditskiy, A.; Peng, H. C.; Qin, D.; Xia, Y. Bimetallic Nanocrystals: Syntheses, Properties, and Applications. *Chem. Rev.* **2016**, *116*, 10414–10472.
- (15) Fichthorn, K. A. Theory of Anisotropic Metal Nanostructures. *Chem. Rev.* **2023**, *123*, 4146–4183.
- (16) Huang, X.; Feng, J.; Hu, S.; Xu, B.; Hao, M.; Liu, X.; Wen, Y.; Su, D.; Ji, Y.; Li, Y.; Li, Y.; Huang, Y.; Chan, T.; Hu, Z.; Tian, N.; Shao, Q.; Huang, X. Regioselective Epitaxial Growth of Metallic Heterostructures. *Nat. Nanotechnol.* **2024**, *19*, 1306–1315.
- (17) Chen, Q.; Lu, Y.; Yang, Y.; Chang, L.; Li, Y.; Yang, Y.; He, Z.; Liu, J.; Ni, Y.; Yu, S. Stress-Induced Ordering Evolution of 1D Segmented Heteronanostructures and Their Chemical Post-Transformations. *Nat. Commun.* **2024**, *15*, 3208.

- (18) He, Z.; Yang, Y.; Liu, J. W.; Yu, S. H. Emerging Tellurium Nanostructures: Controllable Synthesis and Their Applications. *Chem. Soc. Rev.* **2017**, *46*, 2732–2753.
- (19) Feng, Y.; Ji, Y.; Zhang, Y.; Shao, Q.; Xu, Y.; Li, Y.; Huang, X. Synthesis of Noble Metal Chalcogenides via Cation Exchange Reactions. *Nat. Synth.* **2022**, *1*, 626–634.
- (20) Yu, J.; Yin, Y.; Huang, W. Engineered Interfaces for Heterostructured Intermetallic Nanomaterials. *Nat. Synth.* **2023**, *2*, 749–756.
- (21) Bu, L.; Zhang, N.; Guo, S.; Zhang, X.; Li, J.; Yao, J.; Wu, T.; Lu, G.; Ma, J.-Y.; Su, D.; Huang, X. Biaxially Strained PtPb/Pt Core/Shell Nanoplate Boosts Oxygen Reduction Catalysis. *Science* **2016**, *354*, 1410–1414.
- (22) Escudero-Escribano, M.; Malacrida, P.; Hansen, Ma. H.; Vej-Hansen, U. G.; Velázquez-Palenzuela, A.; Tripkovic, V.; Schiøtz, J.; Rossmeisl, J.; Stephens, I. E. L.; Chorkendorff, I. Tuning the Activity of Pt Alloy Electrocatalysts by Means of the Lanthanide Contraction. *Science* **2016**, *352*, 73–76.
- (23) Zerdoumi, R.; Matselko, O.; Rößner, L.; Sarkar, B.; Grin, Y.; Armbrüster, M. Disentangling Electronic and Geometric Effects in Electrocatalysis through Substitution in Isostructural Intermetallic Compounds. *J. Am. Chem. Soc.* **2022**, *144*, 8379–8388.
- (24) Fenton, J. L.; Steimle, B. C.; Schaak, R. E. Exploiting Crystallographic Regioselectivity to Engineer Asymmetric Three-Component Colloidal Nanoparticle Isomers Using Partial Cation Exchange Reactions. *J. Am. Chem. Soc.* **2018**, *140*, 6771–6775.
- (25) Drake, G. A.; Keating, L. P.; Shim, M. Design Principles of Colloidal Nanorod Heterostructures. *Chem. Rev.* **2023**, *123*, 3761–3789.
- (26) Huang, X.; Xu, B.; Feng, J.; Hu, S.; Dou, W.; Yang, T.; Zhan, C.; Liu, S.; Ji, Y.; Li, Y.; Pao, C.-W.; Hu, Z.; Shao, Q.; Huang, X. Continuous Phase Regulation of a Pd-Te Hexagonal Nanoplate Library. *J. Am. Chem. Soc.* **2023**, *145*, 28010–28021.
- (27) De Trizio, L.; Manna, L. Forging Colloidal Nanostructures via Cation Exchange Reactions. *Chem. Rev.* **2016**, *116*, 10852–10887.
- (28) Liu, J.; Zhang, J. Nanointerface Chemistry: Lattice-Mismatch-Directed Synthesis and Application of Hybrid Nanocrystals. *Chem. Rev.* **2020**, *120*, 2123–2170.
- (29) Wei, X.-K.; Jalil, A. R.; Rüßmann, P.; Ando, Y.; Grützmacher, D.; Blügel, S.; Mayer, J. Atomic Diffusion-Induced Polarization and Superconductivity in Topological Insulator-Based Heterostructures. *ACS Nano* **2024**, *18*, 571–580.
- (30) Yamauchi, S. CODATA Key Values for Thermodynamics. *Netsu Sokutei* **2009**, *3*, 61–62.
- (31) Forker, G. M. *Lange's Handbook of Chemistry*; McGraw-Hill: New York, NY, 1979.
- (32) Sen, S.; Bera, S.; Pradhan, N. Maneuvering Tellurium Chemistry to Design Metal-Telluride Heterostructures for Diverse Applications. *Chem. Mater.* **2022**, *34*, 9329–9343.
- (33) Wei, X.-K.; Xiong, D.; Liu, L.; Dunin-Borkowski, R. E. Self-Epitaxial Hetero-Nanolayers and Surface Atom Reconstruction in Electrocatalytic Nickel Phosphides. *ACS Appl. Mater. Interfaces* **2020**, *12*, 21616–21622.
- (34) Sadtler, B.; Demchenko, D. O.; Zheng, H.; Hughes, S. M.; Merkle, M. G.; Dahmen, U.; Wang, L.-W.; Alivisatos, A. P. Selective Facet Reactivity during Cation Exchange in Cadmium Sulfide Nanorods. *J. Am. Chem. Soc.* **2009**, *131*, 5285–5293.
- (35) Da, P.; Zheng, Y.; Hu, Y.; Wu, Z.; Zhao, H.; Wei, Y.; Guo, L.; Wang, J.; Wei, Y.; Xi, S.; Yan, C.-H.; Xi, P. Synthesis of Bandgap-Tunable Transition Metal Sulfides Through Gas-Phase Cation Exchange-Induced Topological Transformation. *Angew. Chem., Int. Ed.* **2023**, *62*, No. e202301802.
- (36) Ferrin, P.; Mavrikakis, M. Structure Sensitivity of Methanol Electrooxidation on Transition Metals. *J. Am. Chem. Soc.* **2009**, *131*, 14381–14389.



CAS BIOFINDER DISCOVERY PLATFORM™

## STOP DIGGING THROUGH DATA — START MAKING DISCOVERIES

CAS BioFinder helps you find the right biological insights in seconds

Start your search

